Applied Physics A (2022) 128:187
https://doi.org/10.1007/s00339-022-05333-2

Applied Physics A
Materials Science & Processing

Investigation of the exuberant cavitation bubble and shock wave dynamics in pulsed laser ablation of copper in distilled water

Prahlad K. Baruah[1] · Arpita Nath[2] · Ashwini K. Sharma[3] · Alika Khare[3]

Received: 12 August 2021 / Accepted: 24 January 2022 / Published online: 10 February 2022
© The Author(s), under exclusive licence to Springer-Verlag GmbH, DE part of Springer Nature 2022

Abstract
Pulsed laser ablation in liquid is a very efficient technique for the synthesis of nanoparticles in colloidal form. In order to maximize the applicability of this technique, it is imperative to understand the dynamics of the underlying phenomena like the generation of cavitation bubbles and shock waves. Hence, in the present work, the dynamics of the cavitation bubbles and shock waves produced during pulsed laser ablation of copper in distilled water is investigated. Two techniques, the shadowgraphy and the beam deflection have been used to characterize these phenomena. The shadowgraphs reveal that in the initial stage, the bubble grows upto a maximum size after which it compresses. It is also observed that the bubbles exhibit secondary oscillations at higher laser fluence. The results obtained for the cavitation bubbles using the beam deflection technique matches well with those obtained by the shadowgraphy technique. Two fluid dynamical models, the modified Rayleigh-Plesset and the Gilmore model have been applied to the temporal evolution data of the bubble obtained from the shadowgraphs to analytically derive the thermodynamical properties of the bubble. Again, the beam deflection technique is applied to study the dynamics of the shock waves and the associated thermodynamics is evaluated by considering its propagation. The extreme high values of pressure and temperature derived at the interface of copper and distilled water can be applied to understand the nucleation of nanoparticles.

Keywords Laser ablation · Cavitation bubbles · Shock waves · Shadowgraphy · Beam deflection

1 Introduction

The mechanism behind the formation of nanoparticles (NPs) via pulsed laser ablation in liquid (PLAL) is one active area of research which although has been rigorously studied, never fails to raise curiosity amongst the researchers [1–5]. The success and popularity of PLAL are largely due to the simplicity involved in the technique. PLAL is a more cost effective technique as compared to its chemical counterparts. It is also known that the NPs synthesized via PLAL are stable and are free from contamination as compared to those synthesized by other methods, especially the chemical ones which require the use of various chemical reagents [6–8]. NPs of any material can be synthesized and there has been successful fabrication of metal, semiconductor, metal oxide, alloys and core–shell NPs using PLAL. The properties of the synthesized NPs can be effectively tuned by varying the laser parameters and the ambient conditions [8–12]. For example, change in the laser fluence has been reported to alter the properties of the NPs [9, 11, 13]. However, in order to understand the origin of such changes, it is extremely important to have a clear picture of the underlying mechanism of PLAL [14, 15]. Over the years, considerable clarity has been achieved in terms of understanding the mechanism of PLAL and many new facets associated with PLAL have come to the fore but there is an unending quest in this direction towards better understanding and increased applications [4, 16, 17].

Once the laser beam is incident onto the target immersed in liquid, target plasma is formed. The plasma formed is confined by the surrounding liquid curtailing the free expansion of the plasma unlike those of under vacuum or in presence of gaseous medium. As a result, the propagation of

✉ Prahlad K. Baruah
prahlad.baruah@sot.pdpu.ac.in; prahladkb@gmail.com

[1] Department of Physics, School of Technology, Pandit Deendayal Energy University, Gandhinagar 382426, India

[2] Department of Physics, National Institute of Technology, 793003 Shillong, Meghalaya, India

[3] Department of Physics, Indian Institute of Technology, Guwahati 781039, India

the plasma gets delayed and there is emission of primary shock waves (SWs). Once the laser pulse is over, the plasma starts cooling down and the hot plasma is replaced by vaporized fluid. At this stage, there are rapid pressure variations and the vaporized fluid forms a bubble or cavity called the cavitation bubble. The behaviour of the SWs and the cavitation bubbles influences the properties of the NPs formed. As such, there have been many endeavours to study the dynamics of the SWs and the cavitation bubbles [15, 18]. For better understanding of the nucleation and growth of NPs via PLAL, studying the thermodynamical aspect of PLAL has been one approach. In order to delve into the thermodynamics of the processes involved, the determination of the pressure and temperature in the vicinity of the target due to the emitted SWs and also the same within the cavitation bubbles is essential. Diagnostic techniques like the shadowgraphy and the beam deflection techniques can be employed to characterize the exuberant nature of the SWs and the cavitation bubbles. In the shadowgraphy technique, image of the bubble and also the SW front as a function of time with respect to the laser pulse is captured to obtain the radius of the bubble and the speed of propagation of the SW to understand the dynamical behaviour [18, 19]. In contrast, in the beam deflection technique the entire time evolution of the SWs and cavitation bubble can be obtained in a single shot of the laser [18, 19]. The beam deflection technique is the simpler technique owing to the low-cost and high sensitivity associated with it. However, the technique is limited by its inability to get visualization of the dynamical evolution of the processes occurring in PLAL. Other techniques such as stroboscopic imaging and X-ray radiography to investigate the dynamics of PLAL and X-ray small angle scattering to study the particle formation inside the cavitation bubble have also been demonstrated [15, 20]. In a recent work, Agrez et al. have used high-speed photography with an adaptive illumination to study the SWs [21]. Han et al. have developed a nanosecond resolution photography system based on PIV dual-head laser and conventional industrial camera to study laser induced cavitation bubbles as well as the shock waves [22]. Geng et al. have recently studied the attenuation characteristics of SWs using time resolved shadowgraphy method [23]. Wilson et al. have very recently demonstrated the use of an interferometric method to obtain direct as well as single-shot measurements of the dynamics of cavitation bubble [24].

There are numerous reports on the study of the bubble expansion and the subsequent release of the NPs from it [20, 25]. However, the thermodynamics within the bubble still needs to be better understood [26]. Hence, in the present work, an attempt has been made to study the dynamics of the cavitation bubbles and the SWs using shadowgraphy and beam deflection technique. The bubble thermodynamics have been studied analytically by the cavitation based modified Rayleigh-Plesset model developed by Lam et al. for incompressible liquid [26]. The same has also been studied by applying the Gilmore model which takes into account the compressibility of the liquid [27]. The dynamics of the SWs have been studied by the beam deflection technique, and the thermodynamical parameters associated with it are estimated.

2 Experimental details

2.1 Shadowgraphy technique

The principle of the shadowgraphy technique lies in the ability of a probe beam to cast the shadow of any obstacle lying in its path onto a camera. The schematic of the experimental setup for recording the images of the cavitation bubbles via shadowgraphy is shown in Fig. 1. The second harmonic of a Q-switched Nd:YAG laser (Spectra-Physics, INDI-HG) having a pulse duration of 7 ns and operated in the single shot mode was focused onto a copper (Cu) target. The Cu target was placed at the bottom of a liquid cell (dimension: 5 cm × 5 cm × 10 cm) made of glass as shown in Fig. 1. The liquid cell was filled with distilled water (DW) to a height of ~ 8 mm above the target. The laser beam was steered suitably using a set of optical components and finally focused using a convex lens (Lens 1) of focal length 10 cm on the target. To record the dynamics of cavitation bubbles via shadowgraphy, a probe laser beam from a continuous wave He:Ne laser (Melles Griot, 05-LHR-991, Power:30 mW, $\lambda = 632.8$ nm) was aligned in a direction perpendicular to the direction of plasma or the pump Nd:YAG laser beam focused onto the target in the vicinity of the ablated region. For proper illumination of the bubbles, the probe beam was expanded using a 10X microscopic objective as shown in Fig. 1. This expanded probe beam (diameter ~ 8 mm) after passing through the breakdown region was imaged onto a fast gated charge coupled device (CCD) camera (PCO Sensicam qe; Number of pixels: 1376(H) × 1040(V); Pixel size: 6.45 µm × 6.45 µm; Scan area: 6.3 mm × 4.8 mm) using another convex lens (Lens 2) of focal length 10 cm to record the shadowgraphic images of the bubbles in the 1:1 configuration.

In order to record the temporal evolution of the bubbles, the CCD camera was triggered appropriately at different interval of time with respect to the laser pulse. The triggering scheme was monitored on a digital storage oscilloscope (DSO; DPO3034; 300 MHz, 2.5 GS/s). The Q-switched pulse from the laser power supply triggered the function generator (Tektronix AFG3102, 1 GS/s, 100 MHz) from which a delayed trigger pulse with respect to the laser signal was generated. This generated pulse was used to trigger the CCD. Thus, shadowgraphic images of the bubbles were

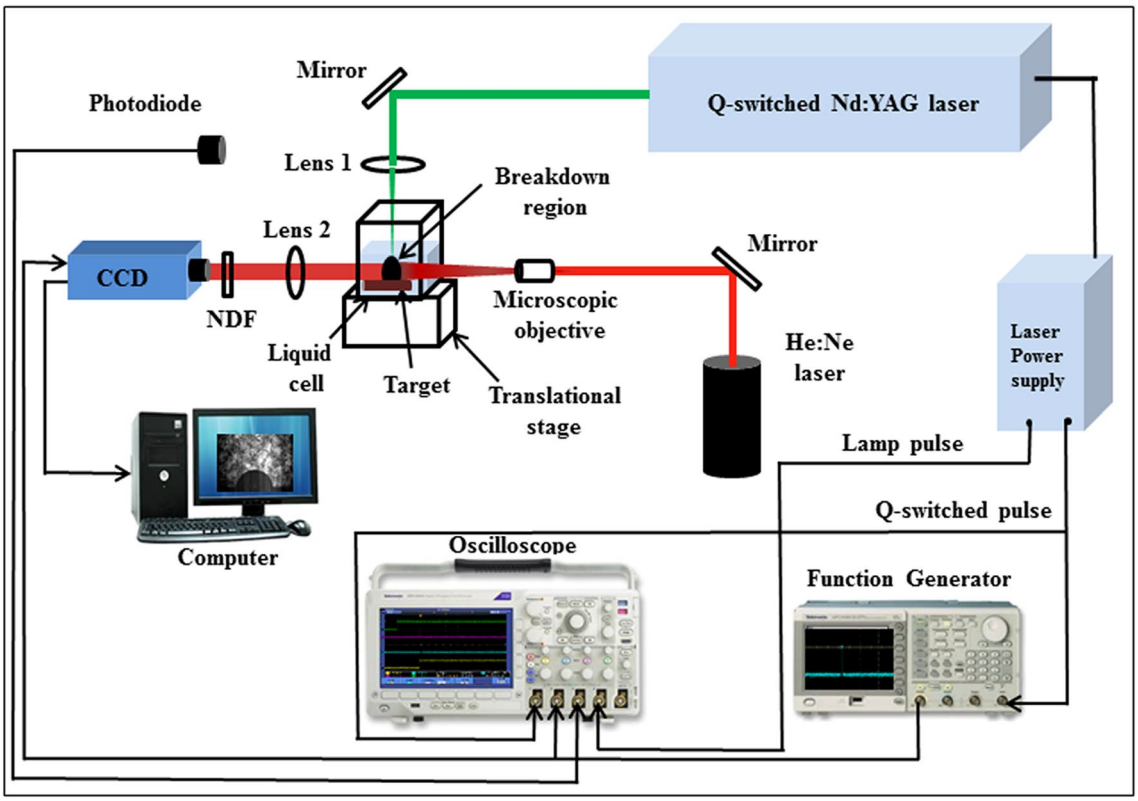

Fig. 1 Schematic of the shadowgraphy setup

captured as a function of time with respect to the laser pulse by delaying the output of the function generator.

Proceeding in this way, the temporal evolution of the cavitation bubbles was recorded. As the experiment was performed in single-shot mode, the recording of the images for each delay time is a separate event with fresh laser shot. The exposure time of the camera was kept fixed at 2 µs and a neutral density filter (NDF; optical density 1.3) was used in front of the camera to avoid its saturation. The experiment was performed at three laser fluences of ~ 10, 16 and 22 J/cm^2.

2.2 Beam deflection technique

The principle of the beam deflection technique involves the deflection of a probe beam due to a refractive index gradient of the medium lying in its path. This deflection of the probe beam is recorded by a position-sensitive detector. Using this technique, the entire time evolution of the SW and cavitation bubble can be obtained in a single shot of laser. The schematic of the beam deflection setup employed for the study of the cavitation bubbles and the shock waves is shown in Fig. 2.

The basic arrangement for the generation of laser induced plasma of the target in DW is same as that of the shadowgraphy technique. The only difference is in the way the probe beam is launched and detected. In the beam deflection technique, a photodiode is used as the detector replacing the CCD camera in the shadowgraphy setup. Here, the He:Ne laser beam (probe beam) is directly made to fall onto a photodiode (P1; Model: 13 DSI 001) which is aligned so that the centre of the beam falls on it giving the maximum signal. The photodiode signal is displayed onto a DSO (through a 50 Ω terminator) interfaced to a computer.

The DSO was triggered with the Nd:YAG laser pulse (employed for the generation of laser induced plasma) through another identical photodiode (P2). For this, a scattered signal at 532 nm of the incident laser was made to fall on P2 and displayed similarly on the DSO along with the signal from P1.

3 Results and discussion

3.1 Dynamics of cavitation bubbles

Figures 3, 4, 5 show some of the shadowgraphic images of the cavitation bubbles captured at various delays with respect to the laser pulse, for laser fluence of 10, 16 and 22 J/cm^2, respectively. Each and every image in these figures is

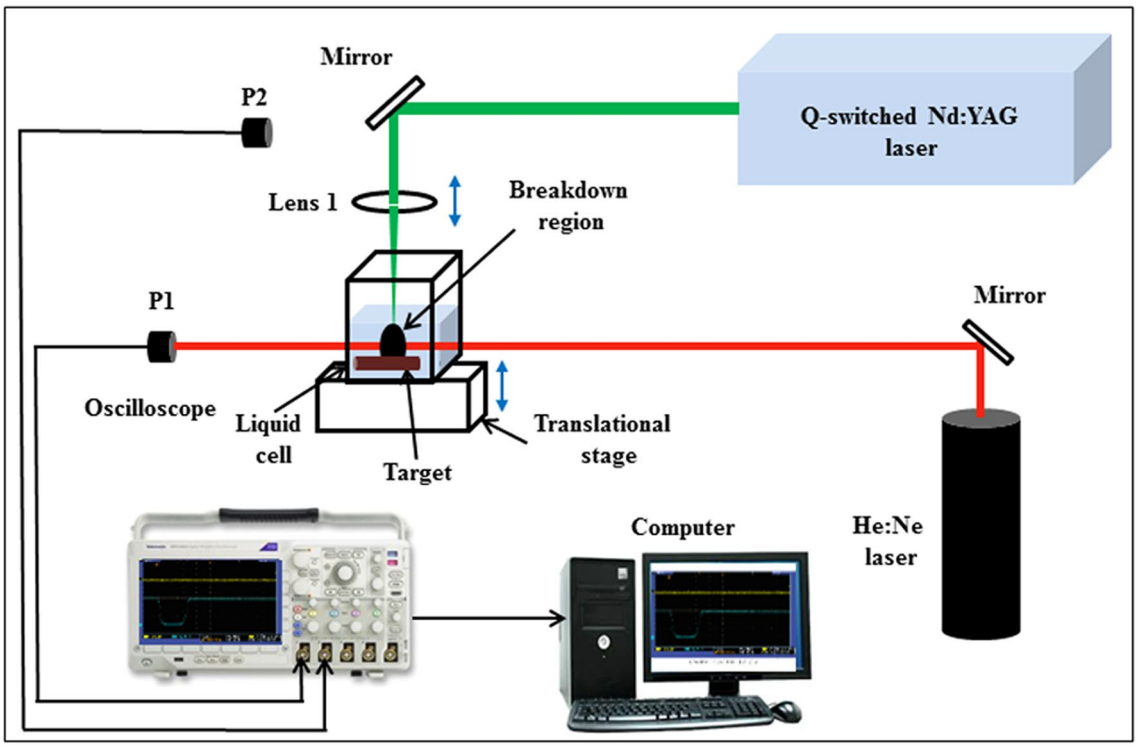

Fig. 2 Schematic of the beam deflection setup

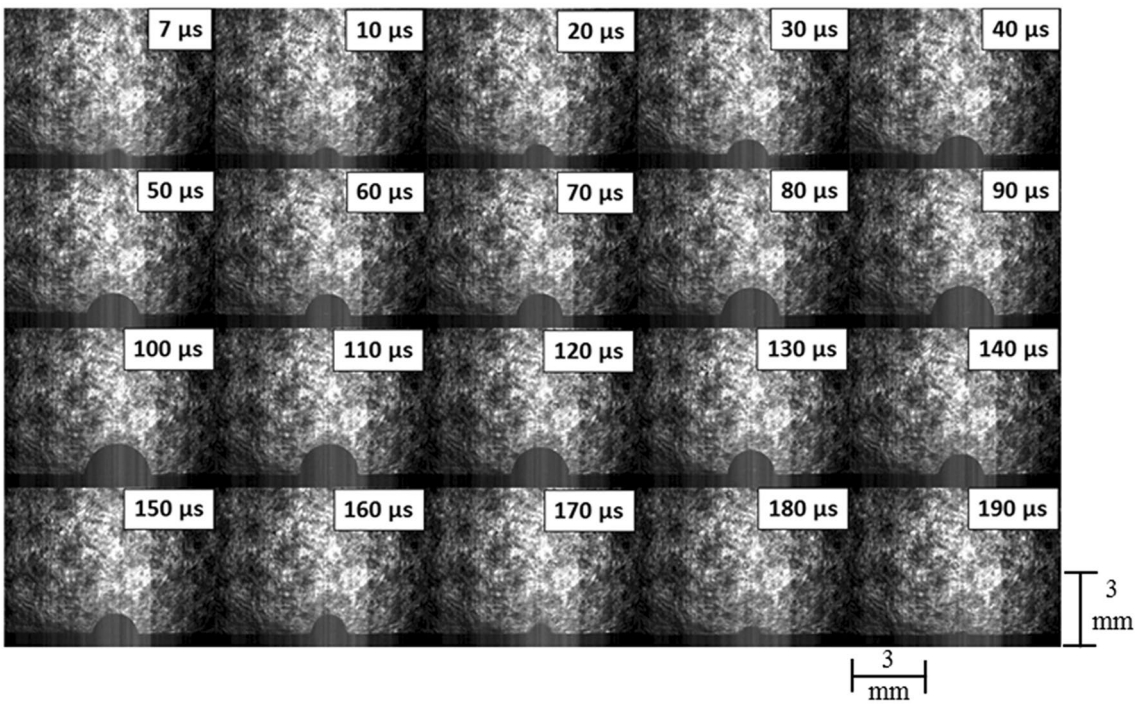

Fig. 3 Shadowgraphs of the cavitation bubbles at laser fluence of ~ 10 J/cm^2

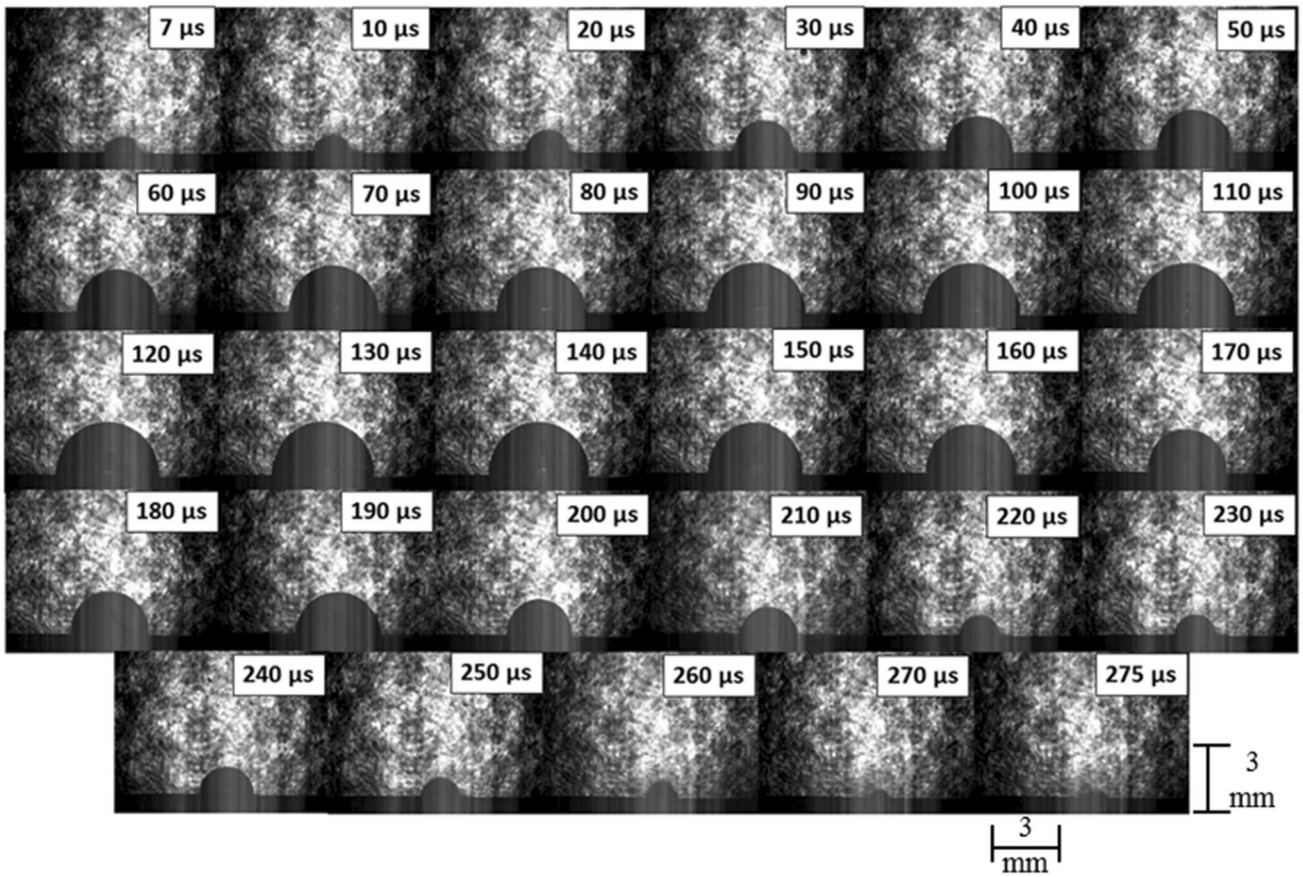

Fig. 4 Shadowgraphs of the cavitation bubbles at laser fluence of ~ 16 J/cm^2

1376 × 1040 pixel^{2,} and the distance was calibrated using a standard scale.

From these images, the bubble radius was measured. Its variation as a function of the delay time with respect to the laser pulse is shown in Fig. 6 for all the three laser fluences. The values shown in the figure are the average over images taken for 20 shots of laser. At ~ 10 J/cm^2, it is observed that the bubble starts expanding due to the inertia of the vaporized species present inside and reaches a maximum radius of 1.5 mm at a delay time of 100 µs with respect to the laser pulse. This is followed by a stage in which the bubble starts compressing in order to maintain the pressure with the hydrostatic pressure of the surrounding liquid. During this stage, the radius of the bubble continues to decrease and it decays completely after 190 µs. The same trend of increase upto a maximum radius followed by compression is also observed at higher fluences of ~ 16 and 22 J/cm^2.

For these higher fluences, the bubble expands upto a maximum radius of 2.5 and 3.4 mm, respectively, at the same delay time of 125 µs. However, at both ~ 16 and 22 J/cm^2, after attainment of maximum bubble radius, the bubble radius decreases and then increases again before dying out completely beyond 275 and 325 µs, respectively. The first increase in the bubble radius and its collapse is generally referred to as the first oscillation of the bubble. [28, 29] The subsequent increase followed by a decrease in the bubble radius which is observed in the case of higher fluences is the second oscillation of cavitation bubble. [28, 29] Thus, from the shadowgraphs of the bubbles at different delay time, it is observed that at lower fluence of ~ 10 J/cm^2, there is no second oscillation of the bubble. However, at higher fluence of ~ 16 J/cm^2 the second oscillation becomes clear and the same becomes more pronounced for the highest fluence of ~ 22 J/cm^2.

In order to confirm the shadowgraphy results of the slight increase in the bubble radius towards the later stage of the cavitation bubble followed by its complete decay for the higher laser fluences, the beam deflection signals at these conditions were analysed. The beam deflection traces at laser fluences of ~ 10, 16 and 22 J/cm^2, depicted in Fig. 7(a–c) show that the bubble lifetime from the shadowgraphy and beam deflection signal are in reasonably good agreement. The slight variation in the results from the two techniques may be attributed to the following factors. In the BD signal, the change in refractive index due to the formation of cavitation bubble and shockwave deflects the probe beam

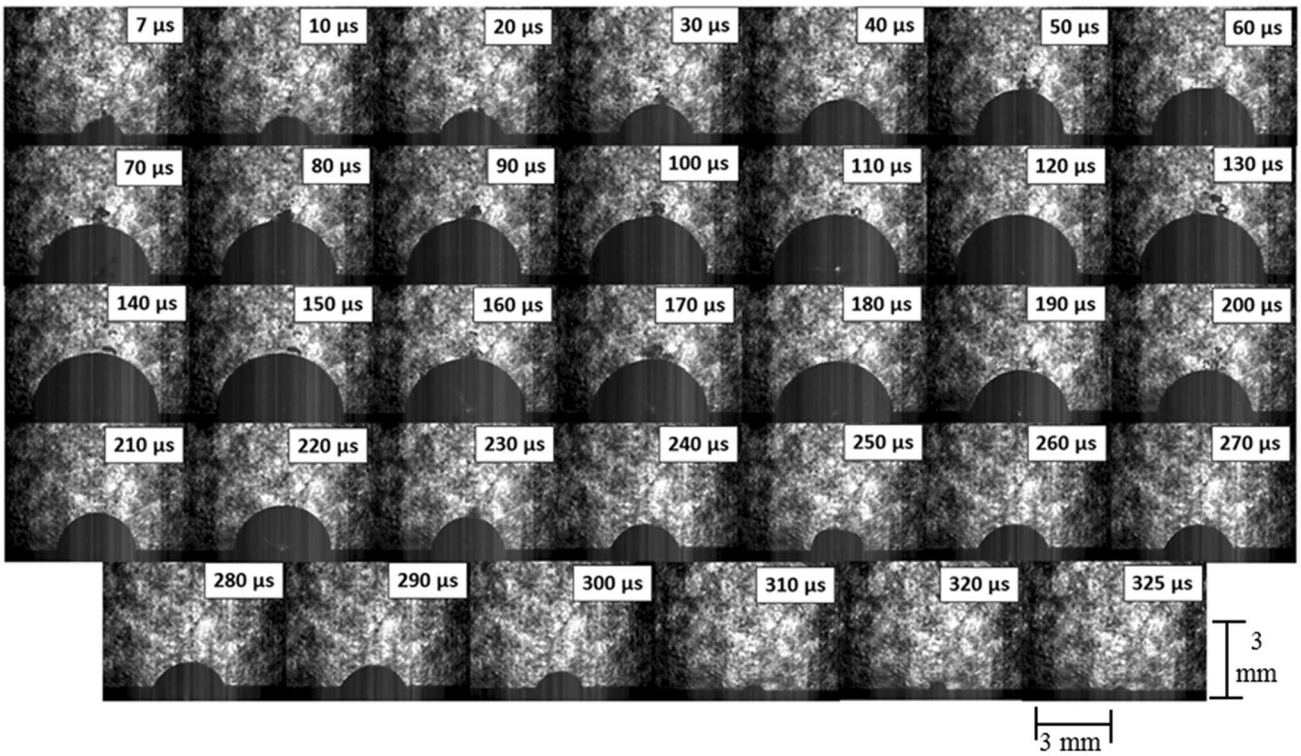

Fig. 5 Shadowgraphs of the cavitation bubbles at laser fluence of ~ 22 J/cm^2

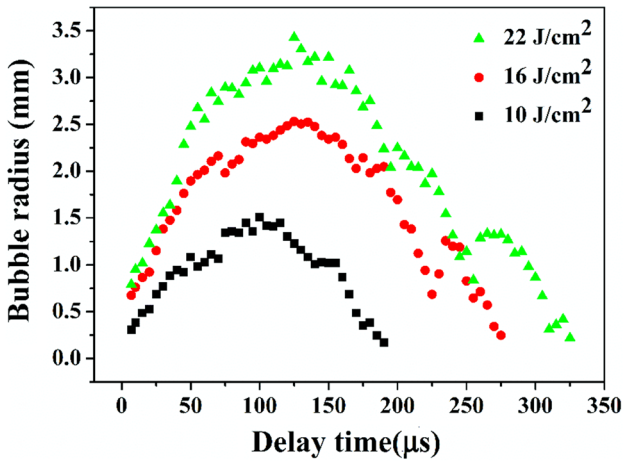

Fig. 6 Variation of bubble radius with time at various laser fluences obtained using shadowgraphy technique

which eventually comes back to its initial dc level. The entire dynamics in the BD setup is recorded in a single shot of laser. However, in the shadowgraphy investigation, the images are recorded at a step size of 5 µs and some information is lost there. Also, as fresh laser shots are used for images at different delays, shot-to-shot variation associated with the laser also induces some variation.

For clarity of understanding, a smooth curve of bubble growth in time and identification of secondary cavitation has been shown in Fig. 7(d) by using an approximate formula reported by Obreschkow et al. [30, 31].

At the fluence of ~ 10 J/cm^2, beam deflection trace does not show any second oscillation of the bubble which is in accordance with that of obtained from the corresponding shadowgraphic images. Interestingly, at ~ 16 and 22 J/cm^2, the speculation about the second oscillation obtained from the shadowgraphs of the bubbles is confirmed by the beam deflection signal which clearly shows the second oscillation. The oscillations are more prominent at the highest fluence of ~ 22 J/cm^2.

In the generation of NPs by the process of PLAL, the properties of NPs, its size in particular, are dependent on the dynamics of the cavitation bubble [18]. So, in order to investigate the influence of laser fluence on the size of the NPs, the temperature and pressure inside the cavitation bubble should be estimated at various fluences. Depending on the magnitude of the pressure and temperature, an idea about the role of laser fluence on the size of the NPs can be ascertained.

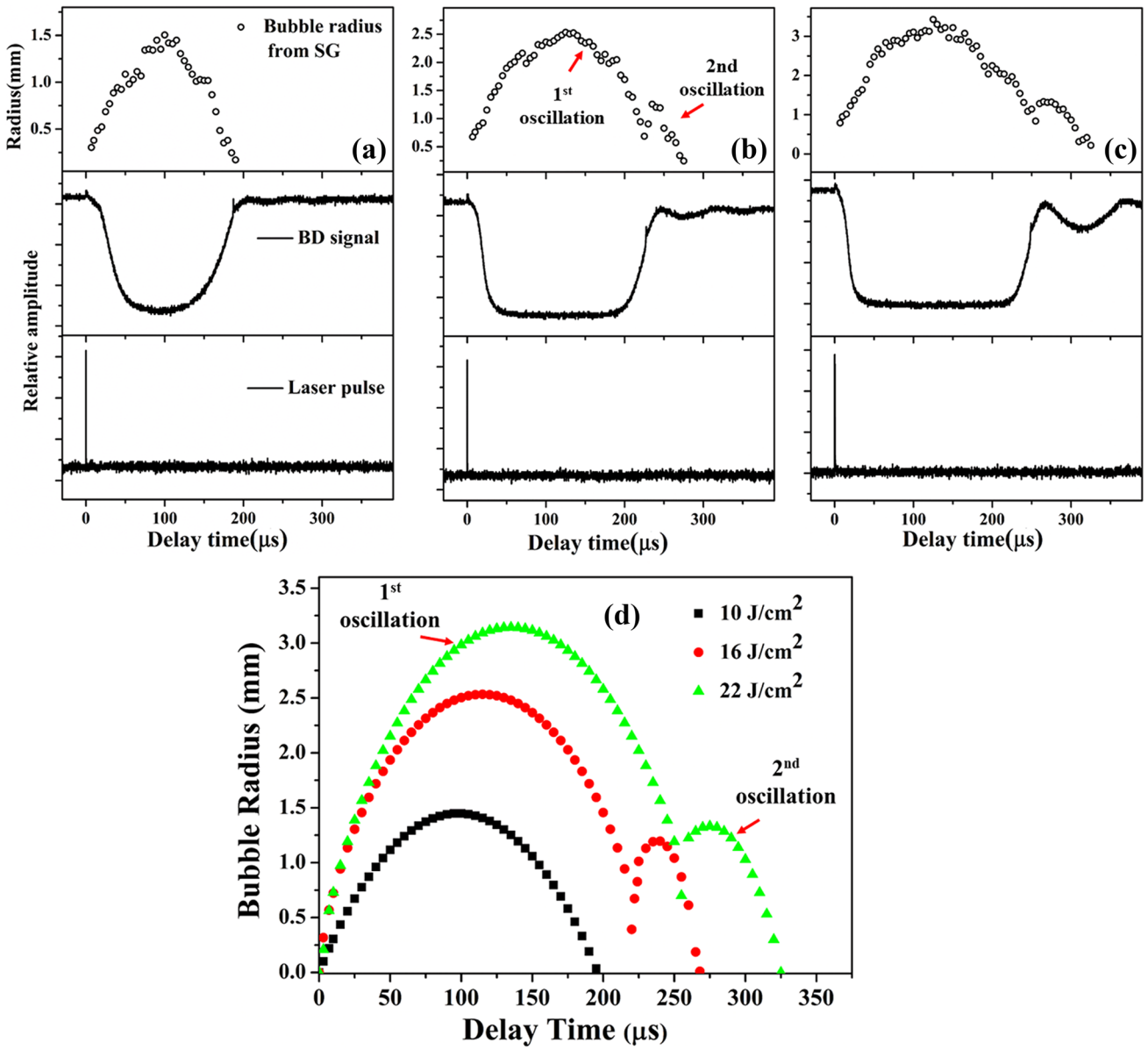

Fig. 7 Comparison of the temporal evolution of cavitation bubbles by shadowgraphy and beam deflection technique at laser fluence of **a** 10, **b** 16 and **c** 22 J/cm^2; **d** Calculated values of Bubble radius as a function of delay time; SG: Shadowgraphy, BD: Beam deflection. The 1st and 2nd oscillation of the cavitation bubble are also marked in the figure

3.2 Rayleigh–Plesset (R-P) model

The temporal evolution of the cavitation bubbles can be utilized to get the pressure profile of the bubbles. Analytically, the dynamics of the cavitation bubble is discussed based on the Rayleigh–Plesset (R-P) equation given by [26, 32, 33].

$$R\ddot{R} + \frac{3}{2}\dot{R}^2 = \frac{1}{\rho}\left[P_B(t) - P_l - \frac{2\sigma}{R} - \frac{4\eta\dot{R}}{R}\right] \quad (1)$$

where R, ρ, P_B, P_l, σ, η represent the bubble radius, mass density of the liquid, internal pressure of the bubble, pressure of the surrounding liquid, liquid surface tension and viscosity of the liquid, respectively. $\dot{R} = \frac{dR}{dt}$ and $\ddot{R} = \frac{d^2R}{dt^2}$. Lam et al. have modified the R-P equation by neglecting the viscous term and the surface effects in the original Equation [26]. For the case of water, it was shown that the ratio of inertial to viscous forces is ~ 10^3 and hence the contribution of the viscous term is negligible [26]. Moreover, the contribution of the inertial term as compared to surface tension is ~ 10^2 and can be neglected. Thus, the modified R-P equation is reduced to [26].

$$R\ddot{R} + \frac{3}{2}\dot{R}^2 = \frac{1}{\rho}\left[P_B(t) - P_l\right] \tag{2}$$

The bubble pressure, P_B as a function of time can be obtained by carrying out an integration of the R-P Eq. (2) which finally gives [26].

$$P_B(t) = (1-\gamma)\left[P_l + \frac{3\rho}{2}\left(\dot{R}_2\frac{C}{R}\right)\right] \tag{3}$$

where γ is the ratio of the heat capacity and C is a constant of integration. Here, it has been assumed that the bubble evolution is adiabatic and the mass transfer to and from the bubble is neglected.

After estimating the pressure profile of the cavitation bubble, the temperature of the bubble as a function of time is derived by using the isentropic equation for an ideal gas which is given by [26, 34].

$$T_B(t) = T_0\left(\frac{P_B(t)}{P_0}\right)^{\frac{\gamma-1}{\gamma}} \tag{4}$$

where T_0 and P_0 are the temperature and pressure corresponding to the time from which the bubble expansion is considered i.e. $t = 7$ µs, in the present study. The value of P_0 is taken from the plot of $P_B(t)$ vs delay time and $T_0 = 647$ K is taken to be the critical temperature of the liquid i.e. water [26]. The reason behind taking the critical temperature as T_0 is that as the bubble is formed, the temperature inside the bubble is below the critical temperature of water and so the critical temperature is considered as the upper limit for T_0 [26]. The value of γ was taken to be 1.22 for water [35].

The pressure and temperature profiles of the cavitation bubbles at laser fluences of ~ 10, 16 and 22 J/cm^2 are depicted in Fig. 8a–c, respectively.

Considering the dynamics of the bubble at the laser fluence of 10 J/cm^2, the bubble pressure starts decreasing from ~ 3.0×10^8 Pa ($t = 7$ µs) and reaches a value of ~ 1.2×10^7 Pa ($t = 35$ µs). After this, the pressure of the bubble varies slowly and reaches a minimum of ~ 2.4×10^6 Pa at a delay of 100 µs (corresponding to the maximum size of the bubble) with respect to the laser pulse. Thereafter, the pressure starts increasing slowly

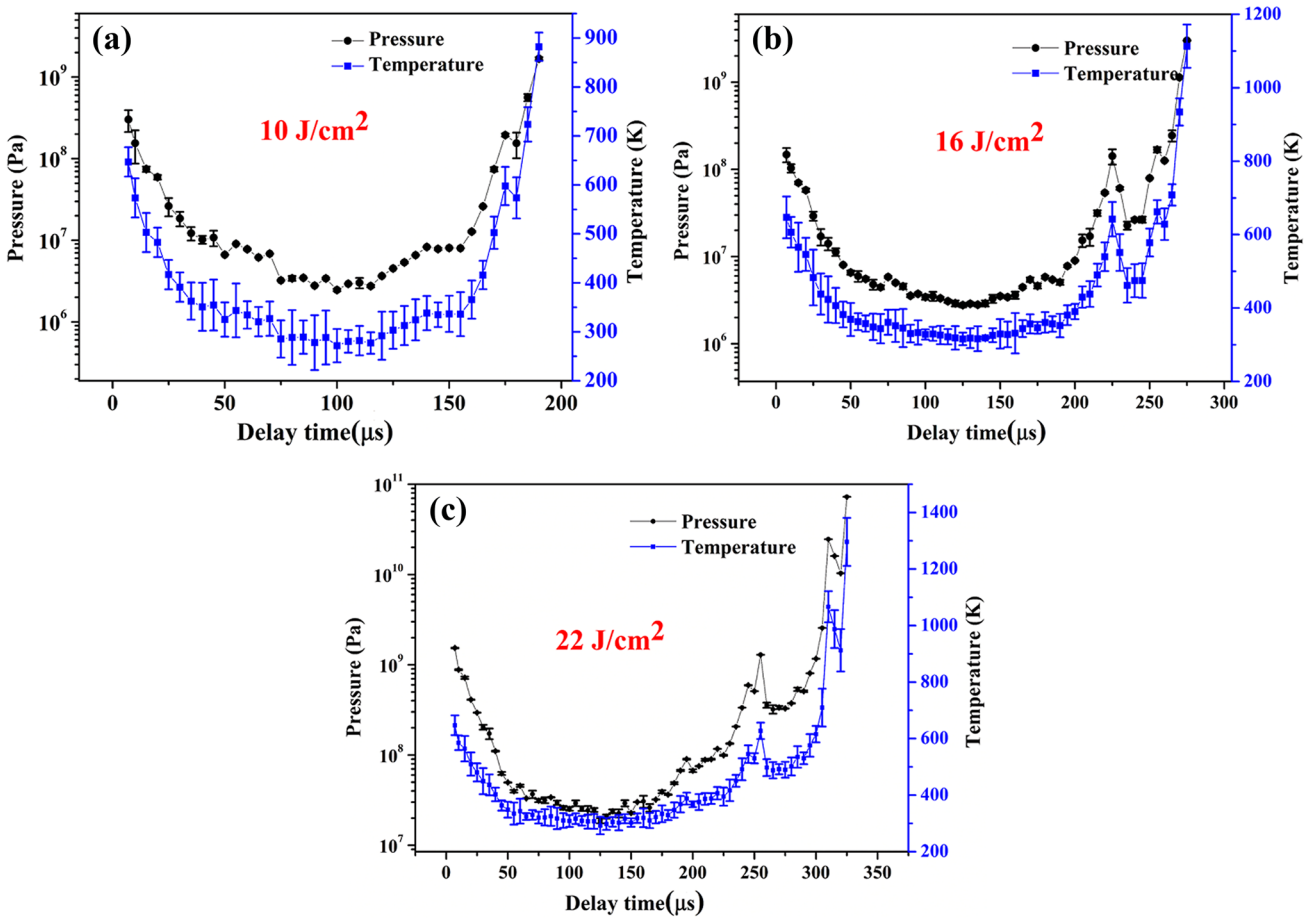

Fig. 8 Pressure and temperature profiles inside the cavitation bubble as a function of time at laser fluence of **a** 10 J/cm^2, **b** 16 J/cm^2, and **c** 22 J/cm^2

upto ~ 1.7×10^7 Pa at 160 µs and then sharply increases upto ~ 1.7×10^9 Pa at 190 µs which denotes the collapse of the bubble. At the fluences of ~ 16 and 22 J/cm^2, the pattern of pressure variation is similar but the low pressure regime is for a prolonged duration of 155 and 165 µs, respectively, as compared to 135 µs for the fluence of ~ 10 J/cm^2. The minimum bubble pressure for ~ 16 J/cm^2 is found to be ~ 2.7×10^6 Pa at 125 µs and that for ~ 22 J/cm^2 is found to be 1.9×10^7 Pa at 125 µs.

As far as the temperature evolution of the bubble as a function of delay time is concerned, the same trend of decrease in the temperature of the bubble with the increase in delay time is observed. The temperature attains a minimum value at the same time as that of minimum pressure, after which the temperature of the bubble starts rising again till it reaches a maximum of nearly 1000 K in the case of ~ 10 J/cm^2 and more than 1000 K for fluences of ~ 16 and 22 J/cm^2. The variation of pressure and temperature inside the cavitation bubbles estimated in the present study is of the same order of magnitude as those reported in pioneering works on cavitation bubbles carried out under similar conditions [35].

3.3 Gilmore model

In this context, it is to be noted that the RP model applied above deals with incompressible flow. This implies that the model is suitable for the bubble dynamics until a few microseconds before the collapse time. During the collapse, as the pressure drastically increases, the compressibility cannot be neglected anymore, and leads to the damping (i.e. energy release through mechanical wave emission) which limits the number of rebound.

As a consequence, if one wants to compute the pressure at the end of the collapse, the Gilmore model (which include the compressibility) is more suitable [27]. To the best of the knowledge of the authors, application of Gilmore model for the estimation of pressure evolution along with spatial evolution (from the bubble wall to different locations in liquid) has not been done so far in the case of PLAL. Also, as reported by Ibrahimkutty et al., most of the NPs are inside the cavitation bubble and get dispersed in liquid during collapse [36]. Therefore, the estimation of the ambient (pressure) conditions at different locations in the surrounding liquid during bubble collapse is pivotal.

Hence, the pressure has also been estimated using the Gilmore model. In this model, the pressure P_B is given as [27].

$$P_B = P_\infty + \frac{R}{r}\left(P - P_\infty\right) + \frac{R\left(r^3 - R^3\right)}{r^4}\left(\frac{\rho_\infty U^2}{2}\right) + \left(\frac{r-R}{r}\right)\left(\frac{U}{c_\infty}\right)\left[\rho_\infty U^2 - 2\left(P - P_\infty\right) - R\left(\frac{dP}{dR}\right)\right] \quad (5)$$

where P_∞, R, ρ_∞ *and* c_∞ represent the hydrostatic pressure, radius of the bubble, density of water and velocity of sound in water, respectively. r is taken as $r = R + x$, where x is the distance from the bubble wall. U is the velocity of the bubble wall and P is the pressure on the walls of the bubble given by $P = p_0\left[\frac{R_0}{R}\right]^{3\gamma}$, where p_0 is the initial pressure inside the bubble prior to collapse and R_0 is the radius before collapse [37]. For our study, p_0 can be very well taken to be the hydrostatic pressure and R_0 as the maximum bubble radius. The value of γ is again taken to be 1.22 for water. Using these values, the pressure has been estimated using the Gilmore model. Figure 9(a–c) shows the pressure profiles at different fluence as a function of distance from the bubble wall and also the delay time with respect to the laser pulse.

At the laser fluence of ~ 10 J/cm^2, at a distance of 50 µm from the bubble wall, the pressure decreases from 2.7×10^7 Pa and reaches a minimum of 1.03×10^5 Pa after which it again rises to 1.98×10^8 Pa. These values follow the same trend as observed in the pressure profiles estimated using the RP model. However, the pressure values are slightly lower as the region of interest is slightly away from the bubble wall and the compressibility of the liquid is also taken into consideration. Similar results are obtained in the case of laser fluences of ~ 16 and 22 J/cm^2 with the values being higher in proportion with the laser fluence used.

3.4 Dynamics of shock waves

Another factor playing an important role in the synthesis of NPs by PLAL, in addition to the cavitation bubbles, is the dynamics of the SWs [14, 18]. Laser ablation of the target immersed in liquid induces SWs in its vicinity which propagates away from the target [7]. The expanded view of beam deflection signal in the early phase as a function of distances above the target for the three fluences of ~ 10, 16 and 22 J/cm^2 is shown in Fig. 10a–c, respectively. The variation in the position of the SW front as a function of distance away from the target, implies the slowing down of the SWs as it moves away from the target.

The SW velocity v_s is determined by considering the temporal evolution of the SW front at different positions with respect to the target surface. The measurement of the SW velocity can be performed by considering the modulation in the He:Ne probe beam at different positions with respect to the target surface as shown in Fig. 11. For this, the target as well as the lens, Lens1 (as shown in Fig. 2), were moved simultaneously along the direction of the source Nd:YAG laser beam and the deflection was recorded as a function of distance from the target. Figure 11 shows the expanded view of the signal recorded at two distances from the target, say X_1 and X_2. As shown in Fig. 11, ΔT is the difference between the delay time T_1 and T_2, with respect to the trigger

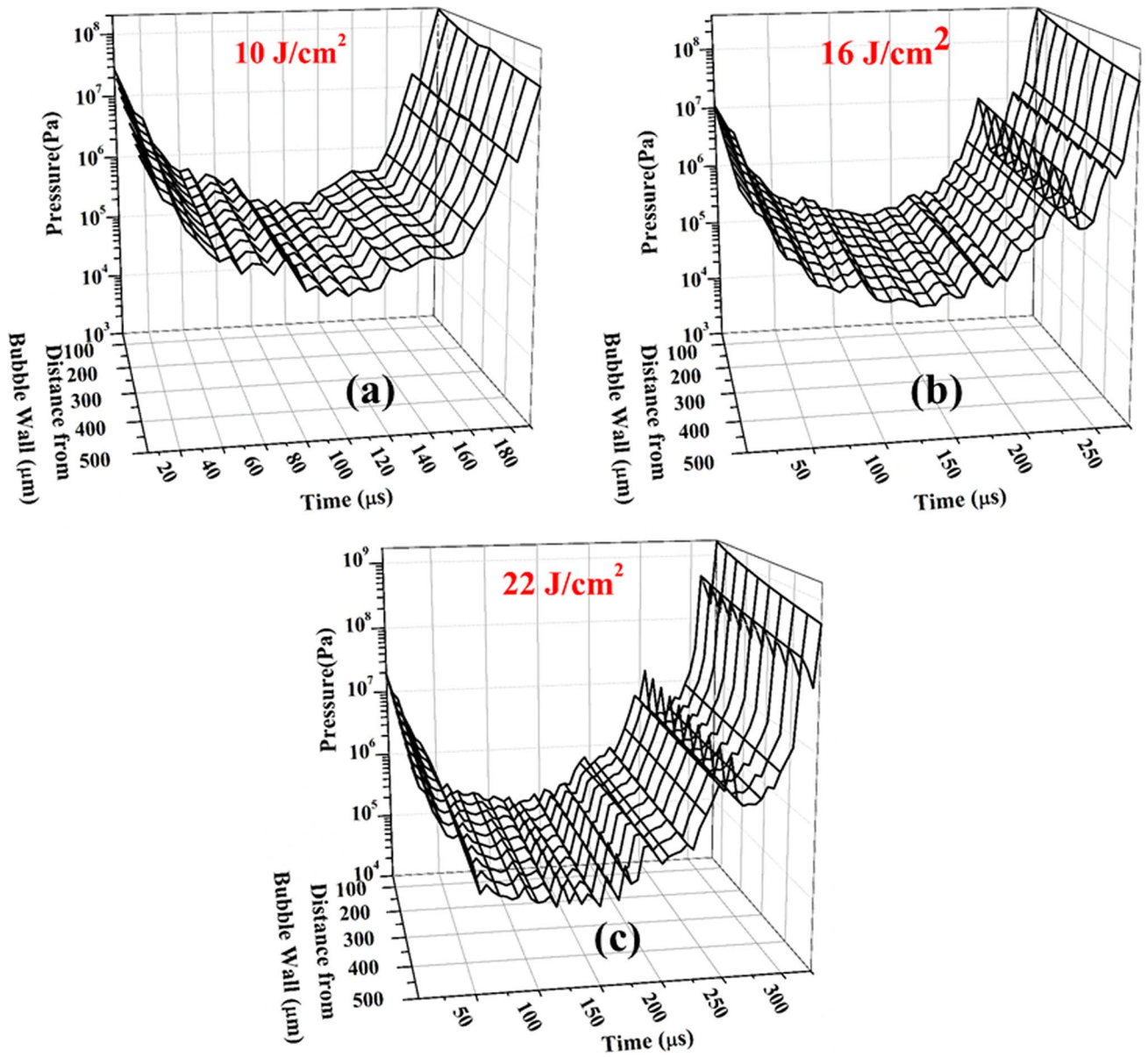

Fig. 9 Pressure profiles as function of distance from the bubble wall and the delay time at laser fluence of **a** 10 J/cm^2, **b** 16 J/cm^2, and **c** 22 J/cm^2

pulse at positions X_1 and X_2, respectively. From ΔT and ΔX, the velocity of the SW can be measured easily.

From the SW velocity, an estimate of the SW pressure can be obtained by the application of Newton's second law across a SW discontinuity. This is given by [38].

$$P_s - P_h = v_s v_p \rho \tag{6}$$

where P_s, P_h, v_s, v_p and ρ are the SW pressure, hydrostatic pressure, SW velocity, particle velocity and density of water, respectively.

The equation of state relates v_s and v_p and this relation is empirically stated as [38, 39].

$$v_s = a + b v_p \tag{7}$$

where $a = 1.48$ km/s is the velocity of sound in water and $b = 2.07$ is a constant.

The SW velocity as a function of distances from the target is shown in Fig. 12a–c for laser fluences of 10, 16 and 22 J/cm [2], respectively.

As the SW propagates away from the target, its velocity decreases in all the three cases. The maximum SW velocity estimated for 10, 16 and 22 J/cm^2 are 8.1×10^3, 9.5×10^3 and 12.1×10^3 m/s, respectively.

The corresponding SW pressures are evaluated using Eq. (6). Now, considering the SW propagation as a

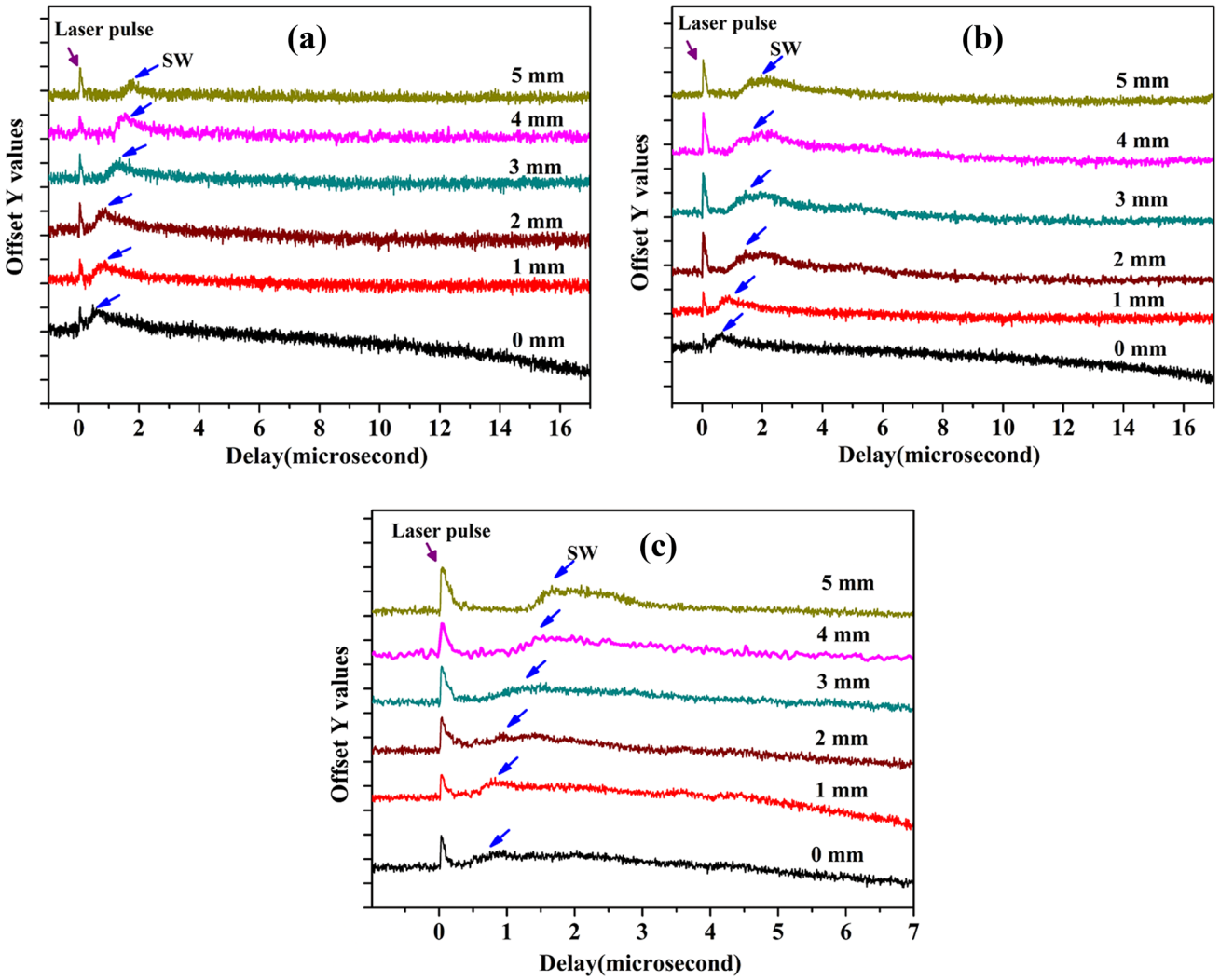

Fig. 10 Beam deflection trace showing the deflection corresponding to the first SW after the laser pulse at laser fluence of **a** 10 J/cm^2, **b** 16 J/cm^2, and **c** 22 J/cm^2

compressible one, the estimation of the temperature from the shock wave pressure is done using Eq. (4) [34].

The variation of the SW pressure and temperature with distance from the target for different laser fluences is depicted in Fig. 12d–f. While the maximum SW pressure is ~ 6.2×10^{10} Pa, the maximum temperature is found to be as high as ~ 3316 K. These extreme conditions favour the formation of NPs and hence a proper understanding of the dynamics of both cavitation bubble and SWs is an absolute necessity to understand well the mechanism of NP synthesis via PLAL.

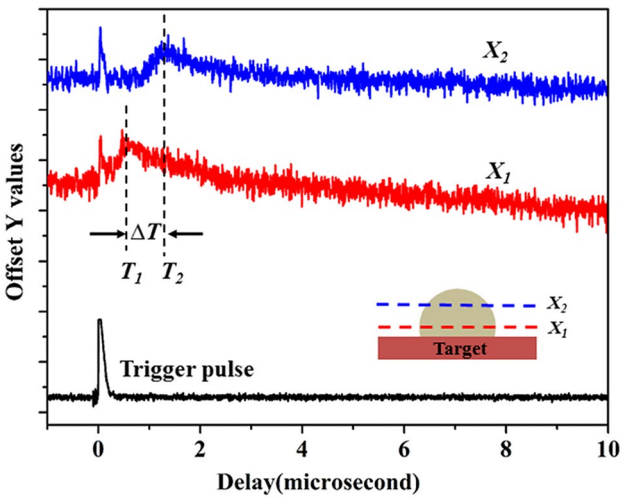

Fig. 11 Beam deflection signal as a function of time at different positions from the target; the inset shows the positions schematically

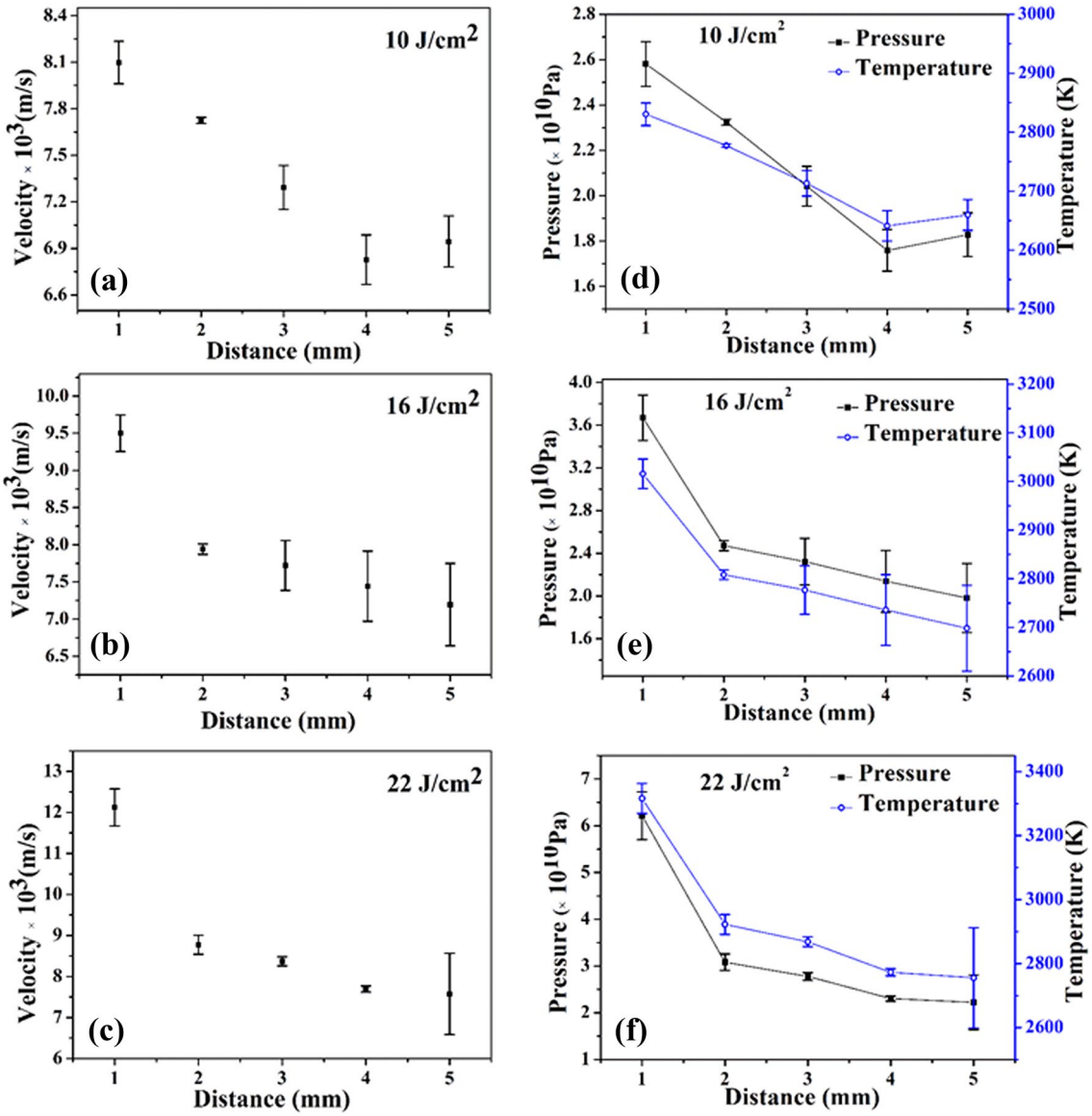

Fig. 12 Shockwave velocity as function of distance from the target at laser fluence of **a** 10, **b** 16 and **c** 22 J/cm^2; Variation of pressure and temperature as a function of distance from the target at laser fluence of **d** 10, **e** 16 and **f** 22 J/cm^2

4 Conclusion

Cavitation bubbles and SWs produced during pulsed laser ablation of a Cu target immersed in DW have been extensively studied in this work. The thermodynamics of the cavitation bubble derived using the temporal evolution of the bubble reveal the variation of high pressure (~ 10^8–10^9 Pa) and temperature (~ 400–1200 K) inside the bubble. The SWs emitted by the laser produced plasma travel at the speed of the order of ~ 10^3 m/s. The pressure and temperature at the interface of Cu and DW have been estimated from the SWs and are found to be as high as ~ 10^{10} Pa and ~ 3000 K. The pressure and temperature estimated for both cavitation bubbles and SWs are found to increase with the increase in incident laser fluence. These calculations can be extended to study the effect of different laser parameters as well as ambient conditions on the properties of the NPs synthesized via PLAL and can help in its better tunability and controlled synthesis.

Acknowledgements The authors would like to acknowledge the Department of Science and Technology (India), for funding through the Project No. SR/S2/HEP-18/2009.

Funding No direct funding was received for this work.

Data availability The data that support the findings of this study are available within the article. If any additional information is required, it will be provided on request.

Declarations

Conflict of interest The authors declare that they have no conflict of interest.

References

1. J. Tomko, S. O'Malley, C. Trout, J. Naddeo, R. Jimenez, J.C. Griepenburg, W. Soliman, D. Bubb, Coll. Surf. A **522**, 368–372 (2017)
2. T. Tsuji, Y. Tsuboi, N. Kitamura, M. Tsuji, Appl. Surf. Sci. **229**(1–4), 365–371 (2004)
3. P. Wagener, S. Ibrahimkutty, A. Menzel, A. Plech, S. Barcikowski, Phys. Chem. Chem. Phys. **15**(9), 3068–3074 (2013)
4. C.-Y. Shih, M.V. Shugaev, C. Wu, L.V. Zhigilei, Phys. Chem. Chem. Phys. **22**(13), 7077–7099 (2020)
5. H. Zeng, X.W. Du, S.C. Singh, S.A. Kulinich, S. Yang, J. He, W. Cai, Adv. Func. Mater. **22**(7), 1333–1353 (2012)
6. Z. Yan, D.B. Chrisey, J. Photochem. Photobiol., C **13**(3), 204–223 (2012)
7. G. Yang, *Laser ablation in liquids: principles and applications in the preparation of nanomaterials* (CRC Press, Florida, 2012)
8. V. Amendola, M. Meneghetti, Phys. Chem. Chem. Phys. **15**(9), 3027–3046 (2013)
9. M.H. Mahdieh, B. Fattahi, Appl. Surf. Sci. **329**, 47–57 (2015)
10. E. Solati, L. Dejam, D. Dorranian, Opt. Laser Technol. **58**, 26–32 (2014)
11. P.K. Baruah, A.K. Sharma, A. Khare, Opt. Laser Technol. **108**, 574–582 (2018)
12. P.K. Baruah, A.K. Sharma, A. Khare, RSC Adv. **9**(26), 15124–15139 (2019)
13. P.K. Baruah, A. Singh, L. Rangan, A.K. Sharma, A. Khare, Appl. Phys. A **126**(3), 1–14 (2020)
14. S. Ibrahimkutty, P. Wagener, T. dos Santos Rolo, D. Karpov, A. Menzel, T. Baumbach, S. Barcikowski, A. Plech, Scient. Rep. **5**, 16313 (2015)
15. S. Reich, P. Schönfeld, P. Wagener, A. Letzel, S. Ibrahimkutty, B. Gökce, S. Barcikowski, A. Menzel, T. dos Santos-Rolo, A. Plech, J. Collo. Interf. Sci. **489**, 106–113 (2017)
16. D. Amans, M. Diouf, J. Lam, G. Ledoux, C. Dujardin, J. Colloid Interface Sci. **489**, 114–125 (2017)
17. C.-Y. Shih, C. Wu, M.V. Shugaev, L.V. Zhigilei, J. Colloid Interface Sci. **489**, 3–17 (2017)
18. J. Chen, X. Li, Y. Gu, H. Wang, X. Song, H. Zeng, J. Colloid Interface Sci. **489**, 38–46 (2017)
19. P. Gregorčič, R. Petkovšek, J. Možina, J. Appl. Phys **102**(9), 094904 (2007)
20. R. Tanabe, T.T. Nguyen, T. Sugiura, Y. Ito, Appl. Surf. Sci. **351**, 327–331 (2015)
21. V. Agrež, T. Požar, Opt. Lett. **45**(6), 1547–1550 (2020)
22. D. Han, R. Yuan, X. Jiang, S. Geng, Q. Zhong, Y. Zhang, Z. Yao, F. Wang, Ultrason. Sonochem. **78**, 105733 (2021)
23. S. Geng, Z. Yao, Q. Zhong, Y. Du, R. Xiao, F. Wang, J. Fluids Eng. **143**(5), 051209 (2021)
24. B.G. Wilson, Z. Fan, R. Sreedasyam, E.L. Botvinick, V. Venugopalan, Opt. Lett. **46**(6), 1409–1412 (2021)
25. M. Dell'Aglio, R. Gaudiuso, O. De Pascale, A. De Giacomo, Appl. Surf. Sci. **348**, 4–9 (2015)
26. J. Lam, J. Lombard, C. Dujardin, G. Ledoux, S. Merabia, D. Amans, Appl. Phys. Lett. **108**(7), 074104 (2016)
27. F. R. Gilmore, https://resolver.caltech.edu/CaltechAUTHORS:Gilmore_fr_26-4 (1952)
28. P. Gregorcic, J. Mozina, Meas. Sci. Technol. **18**(9), 2972 (2007)
29. R. Petkovšek, P. Gregorčič, J. Appl. Phys **102**(4), 044909 (2007)
30. D. Obreschkow, M. Bruderer, M. Farhat, Phys. Rev. E **85**(6), 066303 (2012)
31. S. Wu, Z. Zuo, H.A. Stone, S. Liu, Phys. Rev. Lett. **119**(8), 084501 (2017)
32. R. Lord, Phil. Mag **34**, 94–98 (1917)
33. M.S. Plesset, J. Appl. Mech. **16**, 277–282 (1949)
34. J.D. Anderson Jr., *Fundamentals of aerodynamic* (Tata McGraw-Hill Education, New York, 2010)
35. A. De Giacomo, M. Dell'Aglio, A. Santagata, R. Gaudiuso, O. De Pascale, P. Wagener, G. Messina, G. Compagnini, S. Barcikowski, Phys. Chem. Chem. Phys. **15**(9), 3083–3092 (2013)
36. S. Ibrahimkutty, P. Wagener, A. Menzel, A. Plech, S. Barcikowski, Appl. Phys. Lett. **101**(10), 103104 (2012)
37. R. Hickling, M.S. Plesset, The Phys. Fluid **7**(1), 7–14 (1964)
38. A. Doukas, A. Zweig, J. Frisoli, R. Birngruber, T. Deutsch, Appl. Phys. B **53**(4), 237–245 (1991)
39. P. Harris, H.N. Presles, J. Chem. Phys. **74**(12), 6864–6866 (1981)

Publisher's Note Springer Nature remains neutral with regard to jurisdictional claims in published maps and institutional affiliations.